Microstructure Characterization of Friction Consolidated Copper-Nickel using a Machine Learning Approach

Developing Process to Microstructure Associations

October 2020

Sarah Reehl
Keerti Kappagantula
Elizabeth Kautz
Luke Gosink
Eric Machorro

DISCLAIMER

This report was prepared as an account of work sponsored by an agency of the United States Government. Neither the United States Government nor any agency thereof, nor Battelle Memorial Institute, nor any of their employees, **makes any warranty, express or implied, or assumes any legal liability or responsibility for the accuracy, completeness, or usefulness of any information, apparatus, product, or process disclosed, or represents that its use would not infringe privately owned rights**. Reference herein to any specific commercial product, process, or service by trade name, trademark, manufacturer, or otherwise does not necessarily constitute or imply its endorsement, recommendation, or favoring by the United States Government or any agency thereof, or Battelle Memorial Institute. The views and opinions of authors expressed herein do not necessarily state or reflect those of the United States Government or any agency thereof.

PACIFIC NORTHWEST NATIONAL LABORATORY
operated by
BATTELLE
for the
UNITED STATES DEPARTMENT OF ENERGY
under Contract DE-AC05-76RL01830

Printed in the United States of America

Available to DOE and DOE contractors from
the Office of Scientific and Technical
Information,
P.O. Box 62, Oak Ridge, TN 37831-0062
www.osti.gov
ph: (865) 576-8401
fox: (865) 576-5728
email: reports@osti.gov

Available to the public from the National Technical Information Service
5301 Shawnee Rd., Alexandria, VA 22312
ph: (800) 553-NTIS (6847)
or (703) 605-6000
email: info@ntis.gov
Online ordering: http://www.ntis.gov

Microstructure Characterization of Friction Consolidated Copper-Nickel using a Machine Learning Approach

Developing Process to Microstructure Associations

October 2020

Sarah Reehl
Keerti Kappagantula
Elizabeth Kautz
Luke Gosink
Eric Machorro

1.0   Introduction

Friction consolidation (FC) is a solid phase processing approach where discrete material forms such as powders, chips, nuggets, etc. are densified via shear deformation. The precursors are placed in a billet container and brought in contact with a rotating tool that applying the desirable amount of normal force. Under the combined action of the rotation and normal pressure, the discrete precursor is consolidated through porosity reduction and shear deformation [1]. FC is increasingly being studied as an attractive approach to manufacturing fully dense parts from powder forms owing to its ability to mix, alloy and consolidate difficult-to-process precursors in minimal number of process steps. Material consolidation and deformation in shear consolidation processes have been studied extensively previously for different material combinations previously [2,3]. However, despite the extensive research in this area, understanding of the mechanistic processes in pore consolidation, deformation-induced mixing and material solubility during FC is still evolving [4].

Material development using solid phase processing approaches such as FC is often performed based on research experience/education, which can be biased. Conventional analysis and simulation tools in this area tend to be successful only when material thermodynamic pathways and microstructural evolution sequences resulting from processing are clearly defined or known. They are not as effective for emerging advanced manufacturing technologies where material evolution pathways are not well established. The ability to predict optimal process parameters based on material chemistry and bulk properties is essential to accelerate materials design and processing, as are an understanding of the relevant structure-processing-property relationships. These structure-processing-property-performance relationships are at the core of materials science research. Microstructure characterization provides the link to these four core areas, often through visualizing material microstructure using imaging techniques. However, linking microstructure image data (*i.e.,* micrographs) to variables of interest (*e.g.,* processing parameters, material chemistry) in a reproducible, generalizable, and quantitative manner is a significant challenge. Typically, quantitatively linking image data to processing history relies on significant domain knowledge and manual or subject matter expert (SME)-heuristic based image analysis. Such an approach to image analysis has the potential to be biased, inefficient, and difficult to replicate.

To address this need for an improved approach to linking microstructure image data to a multitude of process parameters, machine learning methods were explored in this study. Machine learning (ML) refers to the process of a computer learning trends in data without human intervention through an iterative training process, and adjusting decisions or actions based on the learning/training process when new data is encountered. Machine learning methods have recently been applied to more challenges in molecular and materials science fields [5]. Applications of such methods include the following: development of accelerated materials design and property prediction [6,7] discovery of structure-property relationships [8], construction of potential energy surfaces for molecular dynamics simulations [9], prediction of atomic scale properties [10] and image classification and analysis [11-14]. Such applications span multiple length scales (macro- to nano-scale) and a variety of material systems (inorganic oxides, electrolytes, polymers, and metals) [15]. The merger of artificial intelligence (AI) with materials science allows for evolution and progression of the research process from a traditional structure-property prediction approach to one that is data-driven. Such a paradigm-shift can accelerate research in the field of materials science through the development of a more autonomous design process and methodology that is more reliable and less subject to

researcher bias and chance discovery. ML methods have previously been applied to further understand microstructures as functions of various parameters, geometric features, or predict material behavior. Some examples: the development of time-temperature-transformation (TTT) diagrams of U-Mo-X type alloys [16], linking microstructural features to processing parameters in a U10Mo fuel [11,12] , inspection of additively manufactured components [17], and optimal AM processes [18] .

A new frontier in machine learning is the ability to analyze smaller data sets, in particular small image data sets. Recent advances have led to developments that allow human-level performance in one-shot learning problems [27]. This advancement is particularly relevant to materials science studies in which researchers are limited to only a few data points/images/etc. Oftentimes, there are limited materials available for analysis due to long lead-time experimentation, or complexity involved in material processing/fabrication.

The dramatic decrease in the cost of computing resources has also made machine learning across many domains. The advent of frameworks such as TensorFlow [19] and Keras [20] allow domain scientists (e.g. materials scientists, nuclear engineers, chemists, physicists) and data scientists alike to apply sophisticated deep learning techniques rapidly to a wide variety of data analysis problems. These advantages enable studies such as the one presented here.

Here, a machine learning approach is presented to characterize microstructures of FC-ed CuNi samples were manufactured using a shear assisted processing and extrusion machine as part of the Solid Phase Processing Initiative research at PNNL. The samples were imaged to identify sample porosity, material mixing, and deformation-assisted solubility prior-to and post-FC using different thermomechanical routes by varying process parameters. In this study, the scanning electron microscopy images were analyzed using different ML algorithms to determine image features used predominantly by the codes for making associations with the process parameters used to manufacture the samples. Trends in process parameter variations associated with corresponding statistically significant changes in image features were identified.

2.0 Methods

2.1 Experimental Data

Process parameters and image data associated with shear consolidated Cu-Ni samples were used in the ML based analysis in this study. It has to be noted that the processing and imaging was not performed in this study; they were performed as part of research efforts in Project 2 of the Thrust 1 of the SPPS Initiative and are summarized here. Copper (Cu) and nickel (Ni) particles, procured from Alfa Aesar with an average particle size of 150 – 420 µm and <125 µm respectively were used in friction consolidation experiments in the study performed by Whalen et al. The Cu and Ni particles were mixed in a 50/50 volume% for 2 h using a rolling mill and compacted initially. Subsequently, the compacted Cu/Ni particle mixture was consolidated using a shear assisted processing and extrusion (ShAPE^{TM}) machine (BOND Technologies, Inc). During compaction in the ShAPE machine, a rotating die impinges on the stationary green compact placed in extrusion container. Owing to the frictional heat generated at the interface of the ShAPE tool and the green compact, the Cu-Ni particle mixture is compacted further as well as plasticized. Three samples were manufactured with varying process times and tool plunge rates as shown in Table 1 below. A type-K thermocouple located 0.5 mm behind the tool face and 5 mm away from the centerline in the radial direction was used to record the temperature at the surface of the deforming Cu-Ni green compact during processing. The variation in torque, power, and force exerted during the process was monitored by the sensors in the instrumented ShAPE machine.

Table 1. Sample nomenclature and process parameters used to manufacture CuNi shear compacted sample using different thermomechanical pathways.

Experimental ID	Sample name	Plunge rate (mm/min)	Final temperature (°C)	Process time (s)	Process data points	No. of SEM images
200183	A	4	500	27	5,436	139
191039	B	4	700	37	51,640	210
191040	C	0.5	700	112	136,416	84

Shear consolidated CuNi samples were sectioned after processing, mounted in epoxy and polished final surface of 0.05 µm using colloidal silica. Scanning electron microscope images of the polished CuNi samples were obtained using a JEOL7600F field emission SEM equipped with an Oxford Instruments Symmetry electron backscatter diffraction (EBSD) CMOS detector and a 170 mm2 X-Max energy dispersive spectrometer (EDS). Data analysis was performed using the Oxford Instruments AZtec Nanoanalysis software package v4.3 along with AZtec Crystal for analysis of the EBSD data.

Process data was in the form of numerical values of force, power, temperature, tool plunge rate, tool rotation rate, and torque as a function process time. These data points (Table 1) were assimilated into process parameter plots corresponding to the different experimentalprocess conditions as shown in Figures 2,5,6,7 below. Image data was in the form on secondary electron images, with corresponding EDS maps identifying the locations of Cu and Ni in a given sample area. SEM images mapped a large area of the samples; the montages corresponding to

different experimental conditions are shown below in Figure 1. It has to be noted that individual images, constituting a montage, were used for data analysis.
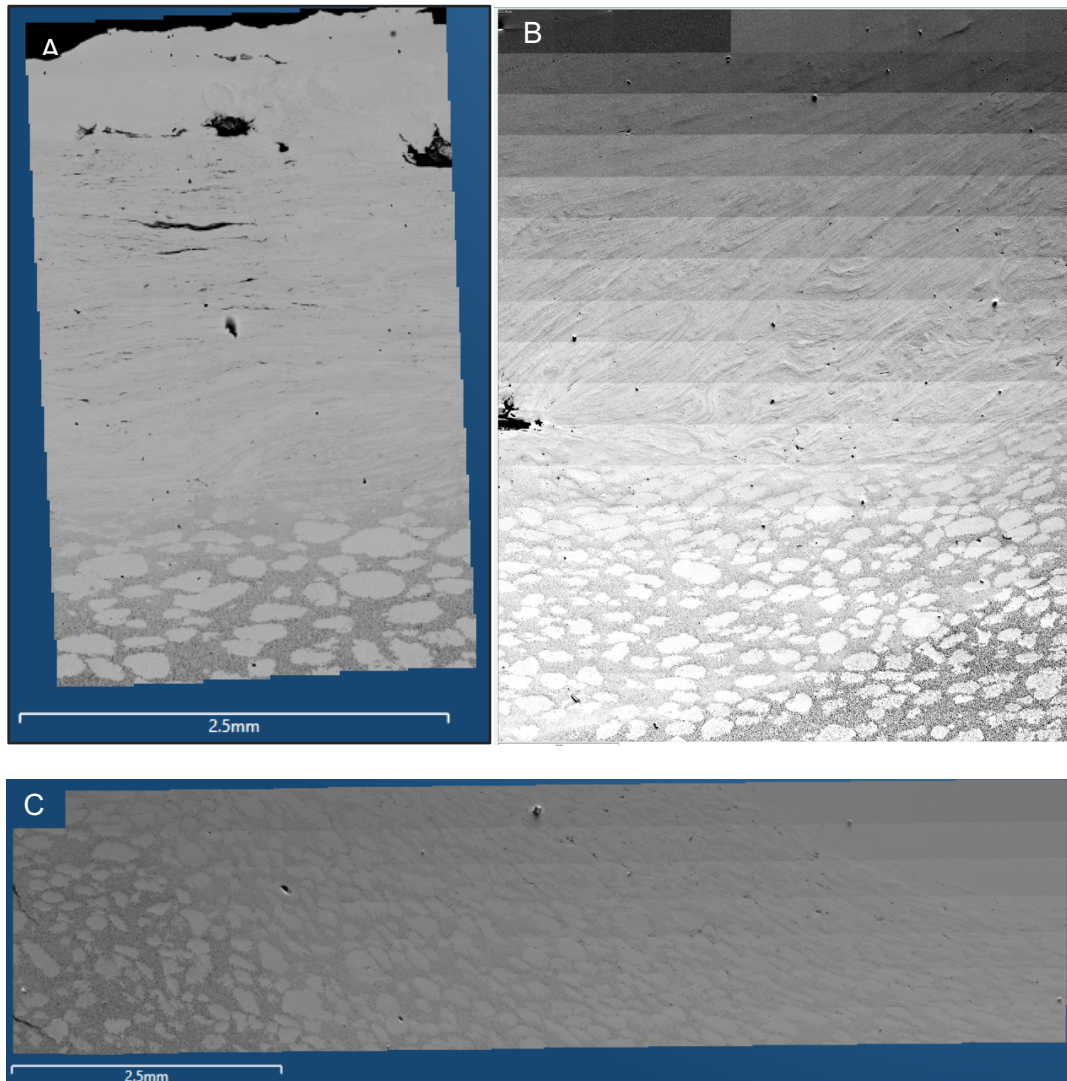
Figure 1. Montages of the SEM images corresponding to the different samples A, B, and C manufactured using the process parameters listed in Table 1.

2.2 Data Analysis & Computational Methods

2.2.1 Preprocessing Images

The images were first preprocessed in MATLAB Version: 9.7.0. The preprocessing approach in this analysis is particularly suited for shape detection in image analysis, specifically separating background from foreground regions in an image in order to make measurements on the foreground microstructures. Preprocessing stages of a representative image in the SEM montage of Sample B is shown below in Figure 2. The first step was a greyscale conversion and anisotropic diffusion that uses 'inter-region smoothing' to effectively reduce noise in the image

while maintaining sharp region boundaries [21]. Next, smoothed image was converted from greyscale to binary where dark pixels are marked as foreground and light pixels were marked as background. The binary conversion occurs with a simple thresholding technique where pixels are classified according to pixel intensity value. Exploratory analysis showed a threshold value of 120, on a scale of 0 to 255, as sufficient in separating background and foreground. The binarized image was then flood-filled [22] on the background pixels, removing any holes left by the thresholding to ensure that foreground objects were fully connected, distinct regions. The connected components were then labeled [23] and available for feature extraction.
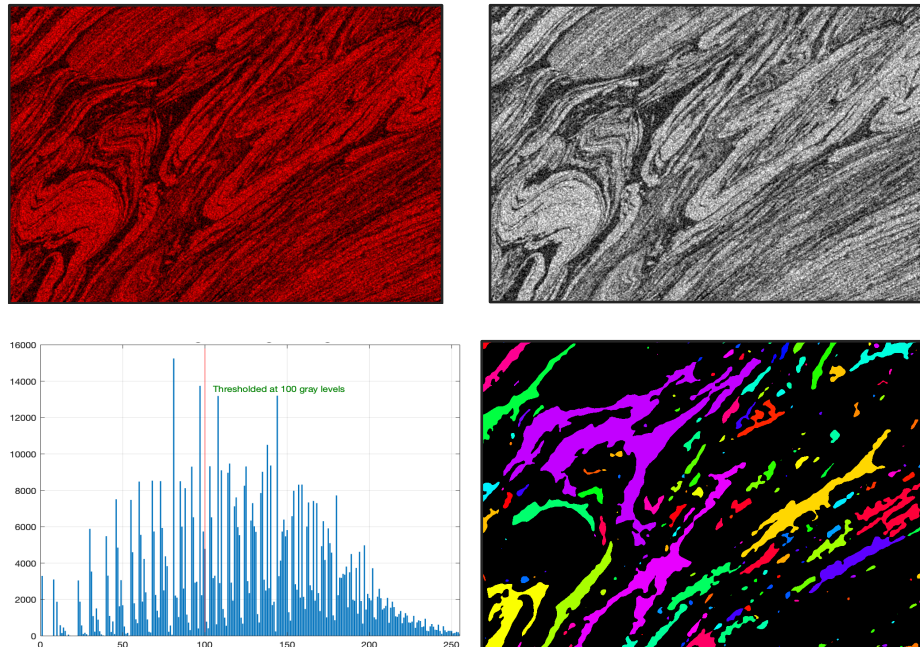
Figure 2. Stages of image analyses of Ni EDS image#89 (Upper Left) from the SEM image of sample B, converted to a grey-scale raw image (Upper Right), whose raw intensities determined (Lower Left) on the basis of which image features were detected (Lower Right), which were used in ML for image classification. Note the comparison between panels on the right.

2.2.2   Computing Features from Microstructural Images

Image features are calculated either from the images or the preprocessed image, obtained from the process described in Section 2.2.1. The raw image features are traditional image statistics derived from measures of raw pixel intensity communicating information on how and where the pixels are distributed. These statistics include the standard deviation of a histogram of oriented gradients (HOG), one-sample Kolmogorov-Smirnov (KS) test, Anderson-Darling (AD) test, Jarque-Bera (JB) test, and a Lilliefors (L) test. HOG is an image feature descriptor that the counts occurrences of gradient orientation in localized portions of an image. In this study, HOG features encode local shape information from regions within an image. KS returns a test decision for the null hypothesis that the data in vector x comes from a standard normal distribution, against the alternative that it does not come from such a distribution, using the one-sample Kolmogorov-Smirnov test. If the distribution is not normal (e.g. bimodal), this indicates that the pixels in the image are likely partially mixed or unmixed. JB returns a test decision for

the null hypothesis that the data in vector comes from a normal distribution with an unknown mean and variance, using the Jarque-Bera test. The alternative hypothesis is that it does not come from such a distribution. L-test returns a test decision for the null hypothesis that the image pixel intensities comes from a distribution in the normal family, against the alternative that it does not come from such a distribution. The preprocessed image features are defined in this study as measures of the labeled shapes detected in each image. These include the number of distinct shapes detected, average minor-axis width, aspect ratio, and average equivalent circular diameter (ECD), a measure of circularity, given by:

$$ECD = \sqrt{4\,A/\pi}$$

Relative depth of a feature was denominated using the image row using where the top of the montage was assumed to be the pseudo-datum. Relative depth was determined from the row position of the image scaled between 0 and 1 which was then converted to microns using the scaling factors for each image. Image features were determined or calculated for each image in the montage of the EDS images corresponding to a sample# (and experimental process parameters). Subsequently, each sample feature dimension was converted from pixels to actual dimensions (µm) in order to correct for any measurement biases such as difference in magnification between samples.

2.2.3 Model Training, Testing, and Validation

Features identified in Section 2.2.1.2 were used to establish an algorithmic relationship between the image features and processing parameters that were used to create the microstructures. The ML algorithm takes as inputs the microstructural image features and predicts a processing parameter of interest such as process temperature or maximum power, defining a mathematical relationship between the feature and process parameter.

Ideally, a wide range of processing parameters would be considered, explicitly relating changes in microstructure to a continuous scale of process parameters with a regression model. However, in light of a limited number of samples corresponding to three distinct processing parameters, a classification analysis is considered. In the classification context, process parameters were described as discrete categories and the algorithmic relationship related observed microstructural features to process parameters by classifying them into process parameter categories. Using the R programming language and the *caret package [24]*, three ML classification models, namely Random Forest (RF), Support Vector Machine (SVM), and K-Nearest Neighbors (KNN) were used to classify the microstructural image features. In total, 348 images were analyzed using 11 total input features, including the 9 image features described above and 2 spatial features related to the position of the image relative to the entire sample. Each montage corresponded to data on two different materials; both sets of EDS images were processed separately.

2.2.4 Degree of Mixing

A quantitative analysis on microstructures as they occur within a larger sample, or on a macroscale, is certainly of interest. While the image processing analysis in the previous section focuses on individual microstructures, preliminary methods were established to determine the distribution of different types of microstructures and where they occur in a sample. The results indicate that a deep learning approach designed for small amounts of data (*i.e.*, Few-Shot Learning) may be useful in an automated macroscale analysis. This approach would bypass the

need for image preprocessing and feature extraction as mentioned above, eliminating known image analysis difficulties like sensitivity to noise, failure to accommodate gradients in contrast level, and poor generalizability.

The design of the few-shot algorithm components additionally leveraged a state-of-the-art image recognition network, ResNet [25]. The ResNet architecture is typically used for image recognition in everyday objects, such as cats and dogs, however this analysis pretrained the network to distinguish between classes of SEM images from a database compiled in [26]. Example images from the database shown in Figure 3 show common SEM images, annotated and labeled into several categories.
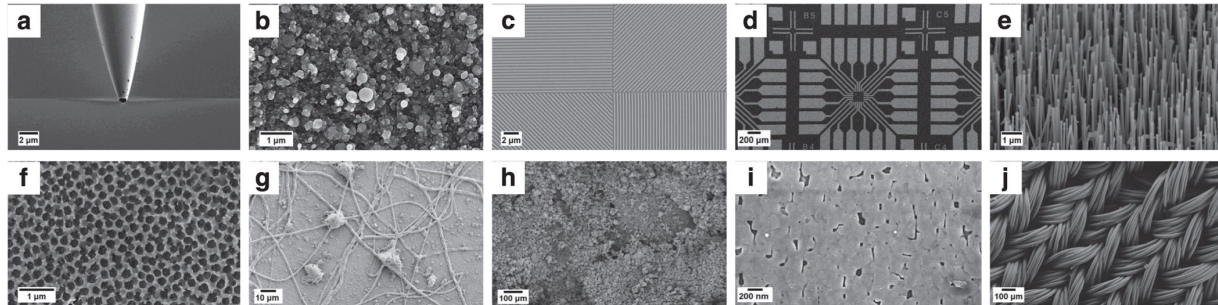
Figure 3. Examples for SEM images from [26] used by ResNet in the Few-Shot analysis. (a) Tips (b) Particles (c) Patterned surfaces (d) MEMS devices and electrodes (e) Nanowires (f) Porous sponge (g) Biological (h) Powder (i) Films and coated surfaces (j) Fibers
After pretraining, the ResNet model is combined with a metric-learning network in a few-shot implementation described by [27]. The algorithm then only needs a 'few' examples of each category to perform classification.

Figure 4below visually describes the three classification categories used for the application of few-shot learning to this data. Each category, "unmixed", "partially mixed", and "mixed" are represented by the images based on SME classification.

"unmixed"   "partially mixed"   "mixed"

Figure 4. Examples of training image data used by the ResNet model combined with metric-learning network in Few-Shot Learning implementation.

Once the categories were defined (Figure 4), all images were fed through the few-shot algorithm and grouped in to one of the three categories or a catch-all 'none of the above' category. A single laptop with a 2.7 GHz Intel Core i7 processor and 16 GB of RAM was used to produce the classification results. The images were also classified as mixed, partially mixed, unmixed by an SME. The accuracy of the Few-Shot algorithm was compared against that of the SME.

3.0   Results & Discussion

3.1   Distribution of Image Categories and Classification Accuracy

The few-shot analysis provided a quantitative assessment of the distribution of image categories as shown in Figure 5. Mixed regions were defined to have no microstructural features, partially mixed regions were seen by the small dimensions of the image features present as filaments or swirls. Unmixed regions were identified by 'blobs' of Cu in a sea of Ni particles with the feature sizes much larger than observed in the partially mixed zone. It has to be noted that the classification accuracy may be improved by providing additional learning images to the Few-Shot Learning algorithm.
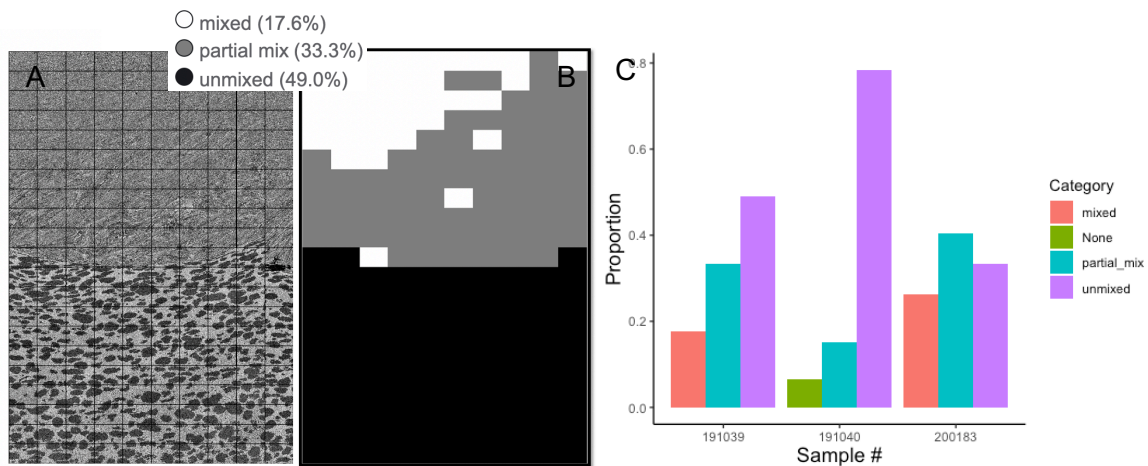
Figure 5. SEM image montage from sample B (Panel A) classified as mixed, partially mixed, and unmixed (Panel B) using Few-Shot Learning technique. Proportion of mixed and unmixed regions in the different SEM images for the different CuNi samples (Panel C).

The preliminary few-shot analysis here lays the groundwork for relating macroscale samples to process parameters. As and when more data are available, the few-shot technique can be refined in multiple ways. With multiple samples taken under the same SEM settings and varying process parameters, the few-shot analysis could potentially link raw images to process parameters directly on a near pixel-by-pixel basis without the need to label every single pixel in a full montage by hand. This approach seems very promising and requires less training/model development time when compared to developing a Deep Learning model from raw image data. A significant challenge in using Deep Learning for this data is the limited number of data sets with varying magnifications, which may bias the network (*i.e.*, it knows the answer based on magnification or blurriness and not image features per se).

Figure 6 reports the classification accuracy of the three ML algorithms used in this study to bin the individual images making up the montages corresponding to different processing parameter experiments. In order to assess the classifier's ability to correctly determine process parameter given the input image features, a repeated k-fold cross validation technique was used in addition to model tuning for optimal performance. The figure below illustrates each classifier's ability to correctly determine process parameters given the input image features across 5 repeats of 10-fold cross validation.
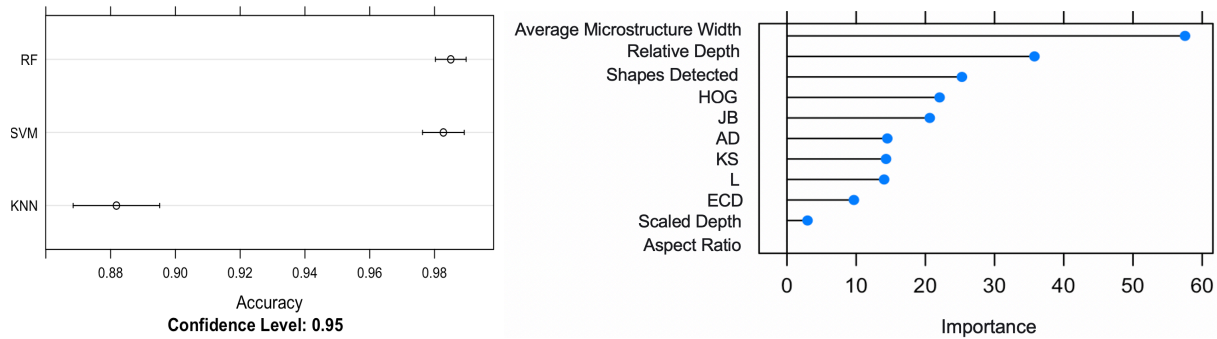
Figure 6. Accuracy of classification for the three different algorithms used in this study (left panel). Note that RF = random forest; SVM = support vector machine, KNN = k-nearest neighbor methods. Importance of the different image features used by the RF (right panel).

The best performing model, on average across all cross validation resamples, was RF with an optimal parameter *mtry*=4, or 4 variables randomly sampled as candidates at each decision point. Additionally, the RF provided an intuitive metric for interpreting which input features were most important in correctly describing process parameter categories. The figure below shows each input feature on the vertical axis and its corresponding importance metric, here the total decrease in node impurities measured by the Gini index from splitting on the variable, on the horizontal axis. The features are effectively ranked as most important to least important from top to bottom. Additionally, the analysis in Section 2.1.1 benefited marginally when image feature calculations were biased to the type of image.

3.2   Associating Process Parameters with Microstructural Features

It was interesting to note that the two most important image features that the RF algorithm used to associate the images with process parameters during classification were average feature width and relative depth of an image in the montage. In order to formally estimate the relationship between filament width and relative depth, a piecewise regression analysis was used. Average feature width was plotted as a function of its location from the montage's pseudo-datum denoted by relative depth as shown in EDS images of Ni were used in determining the feature width and their corresponding location in the montage, meaning that Cu feature dimensions were determined in this exercise. It has to be noted that similar analysis can be performed for Cu EDS images of a sample to determine Ni feature variation as well.

Figure 7 below clearly shows the breakpoint between the partially mixed regions and the unmixed regions in terms of feature width. The relative depth corresponding to the breakpoint can be used to determine the 'depth of mixing' or the thickness of the mixed zone. Image feature sizes <10 µm show that they belong to Cu filaments in the patially mixed regions (tortuous zone) while features in the size range of ~120 µm correspond to the unconsolidated copper particles. Of the three process parameters examined, there is a distinct breakpoint in the Cu feature size which may correspond to the edge of the processed part of the sample. However, these are not compared in this study, since the top of the montage is only taken as a pseudo-datum and 'depth' of the feature is, therefore, only relative.
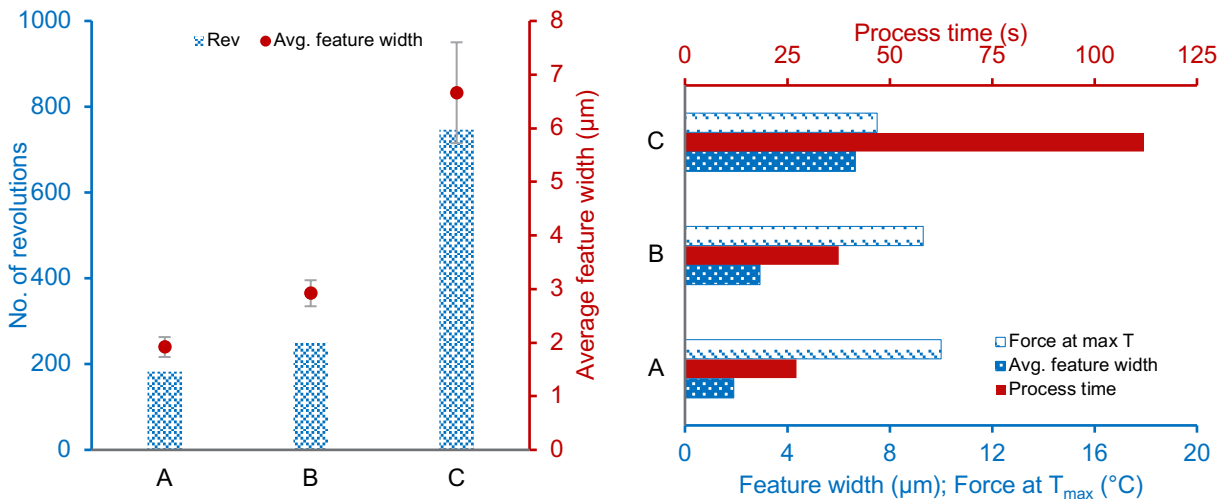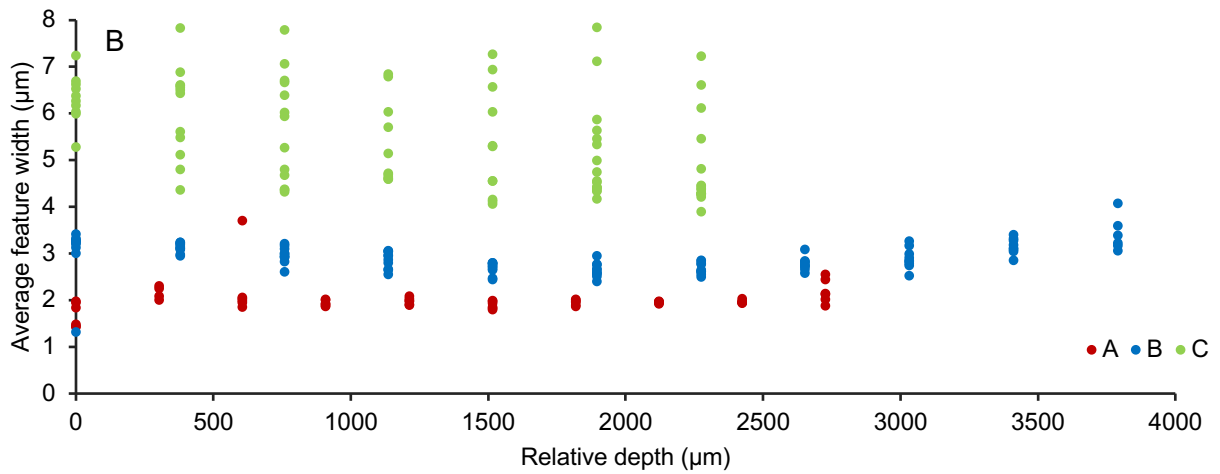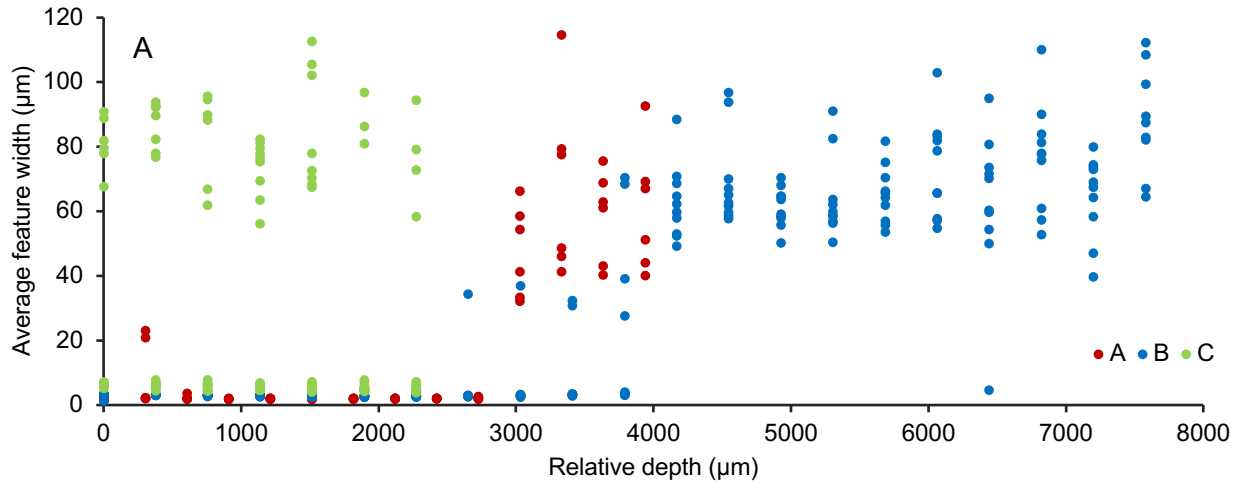
Figure 7. Average feature size as a function of relative depth in the mixed, partially mixed and unmixed regions (as shown in Table 4 and Table 1) of the CuNi SEM images (Top panel), average feature size variation with relative depth in the partially mixed zone (Middle panel), tool revolutions during shear consolidation, average feature depth, process time and consolidation force during sample processing (Lower – Left, Right panels) for the CuNi samples.

What is interesting in Figure 7 is the 'partially mixed' zone where the Cu filament size varies for each sample processed at uniquely different thermomechanical pathways. The Cu-Ni sample A processed for ~27 s at 4 mm/min till a temperature of 500C was attained demonstrated an avergae Cu feature size of 1.92 ± 0.186 µm. On the other hand, the sample B processed for ~37 s at 4 mm/min till 700C showed an average Cu feature size of 2.92 ± 0.243 µm. The largest feature width of 6.661 ± 0.941 µm was seen in the sample C processed for ~115 s till a sample temperature of 700C was reached at a rate of 0.5 mm/min.

A clear association was seen between the process time and the Cu feature size: images from sample processed for longer time demonstrated larger feature widths in the partially mixed zone, while samples processed at the lowest temperatures and shortest duration demonstrated the smallest feature widths (Figure 7- middle and lower-left panels). Examining the plot closely, it can be seen that the Cu feature size distribution was much tighter for the samples A and B, compared to sample C. Average feature width also increased as the number of tool revolutions in the process time increased. On the other hand, extrusion pressure observed during the sample processing was seen to decrease with increasing average feature width.

A generalized linear model (GLM) was used to separately estimate the relationship between relative depth and microstructure feature width. Results from the GLM model analysis are in Table 2. There, δ is a measure of the change in image feature width/µm of relative depth. The preliminary GLM analysis indicates, with statistical significance ($p-value < .05$), that image feature width varies with relative depth for each SEM image montage. Not only does feature width and depth relate to process parameters[1], but the degree to which a sample is fully mixed varies according to the parameters used as well.

Table 2. Generalized Linear Model statistics providing insight into the relationship between the microstructural image feature width and the relative depth of the feature.

Sample	Region	Estimated δ
A	Partially mixed	1.06E-05
A	Unmixed	3.97E-03
B	Partially mixed	-7.59E-05
B	Unmixed	2.29E-03
C	Partially mixed	N/A
C	Unmixed	-2.57E-02

---

[1] more precisely $\mu = {}^{1}/_{\beta + \delta X}$ for X = depth with p-value << .05 for $\delta \neq 0$

4.0 Conclusions & Future Work

This study provided the framework for analyzing scanning electron microscopy and energy dispersive spectroscopy images of friction consolidated copper-nickel powder mixtures using a machine learning framework. Three copper-nickel powder samples friction-consolidated by a shear assisted processing and extrusion (ShAPE^{TM}) machine using different thermomechanical pathways were used as part of developing that framework. Meta-data (*i.e.,* process parameters) associated with the friction processing experiments was examined to identify processing factors of interest such as highest processing temperature.

Initially, transfer learning and few-shot learning techniques were used to classify images as containing completely fully mixed, partially mixed, or unmixed copper-nickel features. Scanning electron microscope images were preprocessed to extract multiple image metrics (*e.g.*, filament width and depth from top of image) Three different machine learning tools, namely Random Forests, K-means Clustering, Support Vector Machines, were used to classify the images into three different classes corresponding to the thermomechanical processing pathways on the basis of the image metrics determined. The random forest classified the images with the highest accuracy. Additionally, the features used predominantly in making the classification were examined. It was seen that the RF algorithm used the average feature width of an image and relative depth of the feature with the highest importance.

The availability of only three different classes of data limited the regression analysis to find the relationships between the ShAPE process parameter factors of interest and the most important image metrics identified by the Random Forests. However, the results showed that the process factors such as number of revolutions, process time, and the force recorded at the highest sample temperature were all correlated with the average feature width of a microstructural image. A generalized linear model analysis was performed to show that with statistical significance (p-values < .05) that image feature width generally varies with depth.

Additional data associated with newer experimental classes (thermomechanical pathways and corresponding scanning electron microscope images) would have provided a higher level of accuracy – enough to discern more precisely the relationships between depth and width within an experimental class and also between classes. The original hypothesis – formed early in this small-scale seedling project - remains: 8-9 samples with distinct process parameter(s) values should allow this mapping between process parameters and microstructural features

Although the analyses herein focused on average feature width in an image and its relative depth in the scanning electron microscope image montage, it is clear that these tools can be straightforwardly generalized in two important areas:

1. Other types of microstructural features such as void size, second phase or additive size morphology and topology which are typically useful indicators of the effect of processing pathways on microstructural evolution.

2. Distinct processing-parameters/settings could be readily distinguished given a more robust set of SEM-images. A practical consequence is that a careful design-of-experiment exercise would maximize the information that could be derived from a give suite of material samples and associated microstructural analyses.

A consequence of these observations is that there are several material systems that this framework could readily be adapted to such as the copper-chromium, copper-niobium,

aluminum-silicon or more complex materials such as heat treatable aluminum alloys. The framework developed here can be employed, completely unmodified, to analyze copper-nickel process parameter-microstructure feature data relationships irrespective of the process used or the image magnification. For example, it would be useful to analyze the copper-nickel images from the RotoDAC experiments performed in the Thrust 2 of the Initiative using the framework developed in this Project to evaluate the microstructural evolution as a function of the process parameters. Furthermore, the broader applications of AIML tools to material informatics problems worth considering further are:

- Integrating the AIML tools with in-site process diagnostics imaging tools and real-time optimal control approaches to managing the material pathways induced by the ShAPE process.

- Using explainability tools to see 'features' used by black-box deep-learning architectures to classify and distinguish microstructural images

- Developing generative methods to manufacture synthetic data to further study microstructural features and provide higher-fidelity bulk-scale models & simulations.

5.0 Works Cited

[1]   David Catalini, Djamel Kaoumi, Anthony P.Reynolds, Glenn J. Grant. 2013. "Friction Consolidations of MA956 Powder." *J. Nuclear Materials* S112-S118.2.

[2]   J. Xu, U. Herr, T. Klassen, and R. S. Averback. 1996. "Formation of supersaturated solid solutionsin the immiscisable Ni-AG systems by mechanical alloyinbg." *J. Appl. Physics.*

[3]   Suryanarayana, C. 2001. *Prog. MAter. Sci* 46: 1-184

[4]   Karoline Sophie Kormout, Reinhard Pippan and Andrea Bachmaier. 2017. "Deformation-Induced Supersatutation in Immiscible Materiasl systems during Hi-Pressure Torsion." *Adv. Engineering Matl.* 19 (4).

[5]   K. T. Butler, D. W. Davies, H. Cartwright, O. Isayev, and A. Walsh, "Machine learning for molecular and materials science," Nature, vol. 559, no. 7715, pp. 547-555, 2018.

[6]   W. Ye, C. Chen, S. Dwaraknath, A. Jain, S. P. Ong, and K. A. Persson, "Harnessing the Materials Project for machine-learning and accelerated discovery," MRS Bulletin, vol. 43, no. 9, pp. 664-669, 2018.

[7]   S. V. Kalinin, B. G. Sumpter, and R. K. Archibald, "Big–deep–smart data in imaging for guiding materials design," Nature materials, vol. 14, no. 10, pp. 973-980, 2015.

[8]   Z. Yang et al., "Deep learning approaches for mining structure-property linkages in high contrast composites from simulation datasets," Computational Materials Science, vol. 151, pp. 278-287, 2018.

[9]   A. J. Ballard et al., "Energy landscapes for machine learning," Physical Chemistry Chemical Physics, vol. 19, no. 20, pp. 12585-12603, 2017.

[10]   A. P. Bartók et al., "Machine learning unifies the modeling of materials and molecules," Science advances, vol. 3, no. 12, p. e1701816, 2017.

[11]   E. Kautz et al., "An image-driven machine learning approach to kinetic modeling of a discontinuous precipitation reaction," Materials Characterization, p. 110379, 2020.

[12]   W. Ma et al., "Image-driven discriminative and generative machine learning algorithms for establishing microstructure-processing relationships," arXiv preprint arXiv:2007.13417, 2020.

[13]   B. L. DeCost and E. A. Holm, "A computer vision approach for automated analysis and classification of microstructural image data," Computational materials science, vol. 110, pp. 126-133, 2015.

[14]   A. Chowdhury, E. Kautz, B. Yener, and D. Lewis, "Image driven machine learning methods for microstructure recognition," Computational Materials Science, vol. 123, pp. 176-187, 2016.

[15]   Y. Liu, T. Zhao, W. Ju, and S. Shi, "Materials discovery and design using machine learning," Journal of Materiomics, vol. 3, no. 3, pp. 159-177, 2017.

[16]   J. M. Johns and D. Burkes, "Development of multilayer perceptron networks for isothermal time temperature transformation prediction of U-Mo-X alloys," Journal of Nuclear Materials, vol. 490, pp. 155-166, 2017.

[17]   B. Zhang, P. Jaiswal, R. Rai, P. Guerrier, and G. Baggs, "Convolutional neural network-based inspection of metal additive manufacturing parts," Rapid Prototyping Journal, 2019.

[18]   N. S. Johnson et al., "Machine Learning for Materials Developments in Metals Additive Manufacturing," arXiv preprint arXiv:2005.05235, 2020.

[19]   M. Abadi et al., "TensorFlow: Large-scale machine learning on heterogeneous systems," 2015.

[20]   A. Gulli and S. Pal, Deep learning with Keras. Packt Publishing Ltd, 2017.

[21]   Malik, P. Perona and J. 1990. "Scale-space and edge detection using ansotropic diffusion." *IEEE Transactions on Pattern Analysis and Machine Intelligence,* 629-639.

[22]   Soille, P. 1999. "Morphological Image Analysis: Principles and Applications,." 173–174. Springer-Verlag.

[23]   Haralick, Robert M., and Linda G. Shapiro. 1992. "Computer and Robot Vision, Volume I." 28-48. Addison-Wesley

[24]   Kuhn, Max. 2020. *caret: Classification and Regression Training. R package version 6.0-86.* https://CRAN.R-project.org/package=caret.

[25]   He, K., Zhang, X., Ren, S., & Sun, J. . 2016. "Deep residual learning for image recognition. ." *In Proceedings of the IEEE conference on computer vision and pattern recognition* pp. 770-778).

[26]   Aversa, R., Modarres, M. H., Cozzini, S., Ciancio, R., & Chiusole, A. 2018. "The first annotated set of scanning electron microscopy images for nanoscience." *Scientific Data* 5: 180172

[27]   Hilliard, N., Phillips, L., Howland, S., Yankov, A., Corley, C. D., & Hodas, N. O. 2018. "Few-shot learning with metric-agnostic conditional embeddings." *arXiv preprint arXiv:* 1802.04376.

**Pacific Northwest
National Laboratory**

902 Battelle Boulevard
P.O. Box 999
Richland, WA 99354
1-888-375-PNNL (7665)

www.pnnl.gov